Heterogeneous nucleation of α-Al primary crystal on $L1_2$ modified $Al_{2.7}Ni_{0.3}Ti$ phase

Yoshimi Watanabe[1]*, Kazunori Maekawa[2], and Hisashi Sato[1]

[1]*Department of Physical Science and Engineering, Graduate School of Engineering, Nagoya Institute of Technology, Nagoya 466-8555, Japan*

[2]*Department of Engineering Physics, Electronics and Mechanics, Graduate School of Engineering, Nagoya Institute of Technology, Nagoya 466-8555, Japan*

* E-mail: yoshimi@nitech.ac.jp

The heterogeneous nucleation of α-Al primary crystal on the $L1_2$ modified $Al_{2.7}Ni_{0.3}Ti$ ($Al_{67}Ni_8Ti_{25}$) phase was investigated. To study the effectiveness of heterogeneous nucleation by the $L1_2$ modified $Al_{2.7}Ni_{0.3}Ti$ phase, an Al-10 vol% $Al_{2.7}Ni_{0.3}Ti$ refiner was fabricated by spark plasma sintering (SPS). It was found that the maximum grain refinement performance can be achieved by the Al-10 vol% $Al_{2.7}Ni_{0.3}Ti$ refiner after a holding time of 690 s. The mechanical properties of pure Al casts were improved by using the Al-10 vol% $Al_{2.7}Ni_{0.3}Ti$ refiner through grain refinement. However, the grain refinement performance is relatively weaker than expected. This is because the Al-10 vol% $Al_{2.7}Ni_{0.3}Ti$ refiner does not have a high thermal stability.

1. Introduction

The refinement of α-Al grains is important for improving the strength of as-cast Al, since as-cast Al has a columnar structure consisting of coarse and elongated grains. Al-Ti, Al-Ti-B, and Al-Ti-C refiners are added in relatively small amounts to refine such a grain structure of Al casts. A number of studies have been carried out to identify the mechanism of α-Al nucleation, and different mechanisms and theories, such as carbide-boride particle theory [1, 2], peritectic theory, phase diagram theory [3, 4], heterogeneous nucleation on Al_3Ti particles [5-7], peritectic hulk theory [8], duplex nucleation theory [8], dendrite remelting [9], and solute theory [10], have been hypothesized. However, many of them have been contradicted. Among them, we believe that the Al_3Ti particles in the refiners act as the centers of heterogeneous nucleation in the mechanism of grain refinement. [11-14], where Al_3Ti has a low-symmetry tetragonal $D0_{22}$ structure and its lattice parameters are a = 0.3851 nm and c = 0.8608 nm, while the Al phase has an fcc structure with a =0.4049 nm.

It is well accepted that an effective refiner contains heterogeneous nucleation sites with good lattice registry with the metal matrix. The plane disregistry δ, [15,16] which is often adopted to discuss favorable heterogeneous nucleation sites, is calculated from the equation

$$\delta_{(hkl)_n}^{(hkl)_s} = \frac{1}{3}\sum_{i=1}^{3}\left\{\left|d[uvw]_s^i \cos\theta - d[uvw]_n^i\right| \Big/ d[uvw]_n^i\right\} \times 100\% \quad , \tag{1}$$

where $(hkl)_s$ and $(hkl)_n$ are the low-index planes of the substrate and nucleated solid, and $[uvw]_s$ and $[uvw]_n$ are the low-index orientations on $(hkl)_s$ and $(hkl)_n$, respectively. Moreover, $d[uvw]_s$ and $d[uvw]_n$ are the interatomic spacing distances along $[uvw]$, and θ is the angle between $[uvw]_s$ and $[uvw]_n$. However, it is unclear why three in-plane directions are considered when evaluating the plane disregistry. Moreover, there are some possibilities to select the third axis. The plane disregistry values of possible crystallographic orientation relationships between Al_3Ti and Al are shown in Table I. As can be seen, the selection of a different third axis results in a different plane disregistry value, even though the crystallographic orientation relationship itself is the same.

Alternatively, the parameter M [17-19], which is approximately proportional to the specific misfit strain energy, will be adopted to discuss the effective nucleant materials. The

parameter M is defined as

$$M = \varepsilon_1^2 + \varepsilon_2^2 + (2/3)\ \varepsilon_1\ \varepsilon_2, \qquad (2)$$

where ε_1 and ε_2 are the principal misfit strains calculated from the principal distortions. Although this consideration has often been applied to epitaxial phenomena, it is potentially applicable to predicting the preferred orientation relationship between two solidified phases. [20] The parameter M values of some crystallographic orientation relationships between Al_3Ti and Al are also shown in Table I. The parameter M is readily applicable to predicting the preferred orientation relationships between the solidified Al and Al_3Ti. That is, favorable heterogeneous nucleation sites for casting could be predicted using the parameter M. On the other hand, it is known that the shape of Al_3Ti particles in the Al-5 mass% Ti ingot is platelet-like [21,22] and the face of Al_3Ti platelets is a $(001)_{Al3Ti}$ plane. [22-24] Therefore, the dominant face of Al_3Ti platelets is not the best plane for heterogeneous nucleation, since it has the largest M value among the above orientation relationships.

To overcome this shortcoming, in our previous studies, high-symmetry $L1_2$ modified $Al_{2.7}Fe_{0.3}Ti$ particles with a lattice constant of $a = 0.393$ nm [25] were used as a heterogeneous nucleant. [26,27] The M value between Al and $Al_{2.7}Fe_{0.3}Ti$ is 2.50×10^{-3}. If a substance with a smaller M value between the solidified phases is used as a heterogeneous nucleant, it is expected that a higher grain refinement performance can be obtained. In this study, therefore, $L1_2$ modified $Al_{2.7}Ni_{0.3}Ti$ ($Al_{67}Ni_8Ti_{25}$) particles with a lattice constant of $a = 0.394$ nm [28] and an M value of 1.93×10^{-3} between Al and $Al_{2.7}Ni_{0.3}Ti$ are used as a heterogeneous nucleant. This is because the M value between $Al_{2.7}Ni_{0.3}Ti$ and Al is smaller than that between $Al_{2.7}Fe_{0.3}Ti$ and Al.

2. Experimental methods

In this study, $L1_2$ modified $Al_{2.7}Ni_{0.3}Ti$ particles were directly prepared by gas atomization. The atomization gas used was Ar and its pressure was 5.0 MPa. The microstructural features of the $Al_{2.7}Ni_{0.3}Ti$ particles were examined using a scanning electron microscopy (SEM) equipped with an energy-dispersive X-ray spectrometer (EDS). The phase of gas-atomized $Al_{2.7}Ni_{0.3}Ti$ particles was analyzed using a Rigaku RINT-2100 X-ray

diffractometer (XRD) with Cu-Kα radiation.

The gas-atomized particles were sieved to obtain a particle size of 75-150 μm, and the sieved $Al_{2.7}Ni_{0.3}Ti$ particles were mixed with pure Al particles (99.9%, 106-180 μm), where the volume fraction of intermetallic compound particles was fixed to 10 vol%. The sintering of the mixed powder by a spark plasma sintering (SPS) apparatus (SPS Syntex SPS-515S) was performed at 500 ^{o}C for 5 min under an applied stress of 45 MPa. The microstructural and phase evolutions of the Al-10 vol% $Al_{2.7}Ni_{0.3}Ti$ refiner were studied by SEM with EDS and XRD, respectively.

To evaluate the grain refinement performance of the prepared refiner, 148.8 g of commercially pure Al ingot (99.99% purity) was melted in an alumina crucible using the electrical resistance furnace at 750 ^{o}C in argon gas atmosphere. After the addition of 1.2 g of the heated refiner into the melt, the melt was stirred with a rod for 30 s, after which no further stirring was carried out. The melt was cast into a cylindrical steel mold of 45 mm inner diameter, 70 mm outer diameter, and 70 mm height after a holding time of 0, 300, 510, 600, 690, or 780 s. Here, the holding time is the time interval from when the stirring was finished to when the melt was cast into the mold.

The classical metallographic route was used to prepare the samples for microstructural analysis. The specimen for grain structure examination was horizontally cut from the bottom part (5 mm from the bottom) of each cast sample. The macrostructural and microstructural features of the casts were studied by optical microscopy after etching the polished surface with a 10% hydrofluoric acid aqueous solution. The linear intercept technique was used to quantify grain size.

For mechanical property characterization, tensile tests and hardness measurements were carried out. Tensile specimens with a reduced gauge section of 4 x 10 mm^2 with a thickness of 6 mm were prepared. Here, the tensile direction is parallel to the radial direction of the casts. Tensile tests were conducted using an Instron-type tester (Shimadzu AG-1/250 kN) at a nominal strain rate of 10^{-3} 1/s. Two or three tensile tests were carried out for each cast. Microhardness measurements were carried out using a Vickers device under an applied load of 1 kgf for 15 s. Seven data from nine measurements at different points of the sample were used to calculate the average microhardness.

3. Results and discussion

3.1 Microstructure of $L1_2$ modified $Al_{2.7}Ni_{0.3}Ti$ particles

The XRD pattern of gas-atomized $Al_{2.7}Ni_{0.3}Ti$ particles is shown in **Fig. 1(a)**. X-ray analysis shows the peak pattern of $L1_2$ modified $Al_{2.7}Ni_{0.3}Ti$, although some unidentified small peaks appear. The lattice constant of the $Al_{2.7}Ni_{0.3}Ti$ is a = 0.3928 nm, which is in agreement with the reported value. [28)]

Figure 2 shows the SEM images of $L1_2$ modified $Al_{2.7}Ni_{0.3}Ti$ particles prepared by gas atomization, where (a)-(d) are the low-magnification photograph, powder surface, cross sections of particles, and high-magnification micrograph showing the cross sections of particles, respectively. From **Figs. 2(a) and 2(b)**, some satellite particles can be observed on the surfaces of coarser particles. From the cross-sectional views shown in **Figs. 2(c) and 2(d)** and the EDS results shown in Table II, the $Al_{2.7}Ni_{0.3}Ti$ particles were formed to consist of two phases, i.e., a gray matrix phase with the stoichiometric chemical composition of $Al_{2.7}Ni_{0.3}Ti$ and a white Ni-rich secondary phase.

The volume fraction of the secondary phase in the gas-atomized $Al_{2.7}Ni_{0.3}Ti$ particles with different sizes is shown in Table III. As can be seen, the small particles have a small amount of secondary phase. The $Al_{2.7}Ni_{0.3}Ti$ particles used as the refiner contain an 8.0 vol% secondary phase.

3.2 Microstructure of Al-10 vol% $Al_{2.7}Ni_{0.3}Ti$ refiner

The XRD pattern and SEM images of the fabricated Al-10 vol% $Al_{2.7}Ni_{0.3}Ti$ refiner are shown in **Figs. 1(b)** and **3**, respectively. It can be seen from **Figs. 1(b)** and **3** that $L1_2$ modified $Al_{2.7}Ni_{0.3}Ti$ particles are successfully embedded in the Al matrix, since there are obvious peaks of $Al_{2.7}Ni_{0.3}Ti$ and Al phases. The magnified microstructure shown in **Fig. 3(b)** reveals that no reaction between the $Al_{2.7}Ni_{0.3}Ti$ particle and the Al matrix occurs at the interface. EDS analysis was carried out in the matrix and particle regions, and the results are shown in Table IV. Matrix and particles were identified to be Al with small amounts of Ti and stoichiometric $Al_{2.7}Ni_{0.3}Ti$ intermetallic compound, respectively. From the magnified microstructure shown in **Fig. 3(b)**, the secondary phase observed in the gas-atomized particles is still found in the Al-10vol%$Al_{2.7}Ni_{0.3}Ti$ refiner, although the refiner was fabricated at elevated temperatures. Therefore, no significant reaction occurs upon heating for a shorter period and the $L1_2$ modified $Al_{2.7}Ni_{0.3}Ti$ particles with a small amount

of secondary phase still remain in the refiner.

3.3 Grain refinement performance of Al-10 vol% $Al_{2.7}Ni_{0.3}Ti$ refiner

By using the Al-10 vol% $Al_{2.7}Ni_{0.3}Ti$ refiner, the grain refinement performance is studied. The macrographs of Al casts refined using the refiner are shown in **Fig. 4**, where holding times in (a)-(f) are 0, 300, 510, 600, 690, and 780 s, respectively. For comparison, the macrostructure of an unrefined pure Al cast is shown in **Fig. 4(g)**. The Al cast without the refiner has coarse and inhomogeneous grains, as shown in **Fig. 4(g)**, and the average grain size is about 3574 μm. On the other hand, the grain size is smaller in the Al cast with the refiner, although the macrostructure retains a columnar structure in the outer region of the cast.

A quantitative analysis of the average grain size is carried out and the results are shown in **Fig. 5** as a function of holding time. The results of the Al cast refined by the Al-10 vol% $Al_{2.7}Fe_{0.3}Ti$ refiner are also shown in this figure. [26] The minimum grain size of 405 μm can be achieved for the cast refined by the Al-10 vol% $Al_{2.7}Ni_{0.3}Ti$ refiner after the holding time of 690 s. This size is about one ninth that of the unrefined cast. As can be seen, a reduced grain refinement performance (fading) is found when the holding time becomes 780 s. Note that a lower grain refinement efficiency is found for the Al-10 vol% $Al_{2.7}Ni_{0.3}Ti$ refiner than for the Al-10 vol% $Al_{2.7}Fe_{0.3}Ti$ refiner. This phenomenon cannot be explained by simple lattice matching between the heterogeneous nucleant and the nucleated solid, since the M value between $Al_{2.7}Ni_{0.3}Ti$ and Al, $M = 1.93 \times 10^{-3}$, is smaller than that between $Al_{2.7}Fe_{0.3}Ti$ and Al, 2.50×10^{-3}. This will be discussed later.

3.4 Mechanical properties of Al casts

Figure 6 shows the nominal stress-nominal strain curves of Al casts manufactured without and with the Al-10 vol% $Al_{2.7}Ni_{0.3}Ti$ refiner after the holding time of 690 s. It is clear that the refined Al cast has a higher strength. 0.2% proof stress and tensile strength are evaluated from these stress-strain curves and results are listed in Table V. The microhardness values of the refined and unrefined Al casts are also listed in Table V. The microhardness of the Al cast with the refiner is higher than that of the cast without the refiner. By using the Al-10 vol% $Al_{2.7}Ni_{0.3}Ti$ refiner, the mechanical properties of pure Al casts can

be improved by grain refinement.

3.5 Thermal stability of $Al_{2.7}Ni_{0.3}Ti$ phase in refiner

In this section, we would like to discuss why the grain refinement efficiency of the Al-10 vol% $Al_{2.7}Ni_{0.3}Ti$ refiner is not superior to that of the Al-10 vol% $Al_{2.7}Fe_{0.3}Ti$ refiner. The Al-10 vol% $Al_{2.7}Ni_{0.3}Ti$ refiner was fabricated by the SPS route, which can be achieved in the unequilibrium state, since sintering can be carried out at a low temperature with short heating, holding, and cooling times. [29,30] In our previous study, the decomposition phenomenon of the $Al_{2.7}Fe_{0.3}Ti$ phase in the Al-10 vol% $Al_{2.7}Fe_{0.3}Ti$ refiner fabricated by SPS was studied. [27] It has been found that the thermal stability of the heterogeneous nucleation site also affects the grain refinement performance. It is, therefore, expected that the decomposition phenomenon will occur more rapidly for the Al-10 vol%$Al_{2.7}Ni_{0.3}Ti$ refiner.

Next, the thermal stability of the $Al_{2.7}Ni_{0.3}Ti$ phase in the Al-10 vol% $Al_{2.7}Ni_{0.3}Ti$ refiner is investigated. For this purpose, the Al-10 vol% $Al_{2.7}Ni_{0.3}Ti$ refiner was heated at 750 ºC for 90, 300, or 510 s. **Figures 7(a)-7(c)** show the microstructures of the Al-10 vol% $Al_{2.7}Ni_{0.3}Ti$ refiner heated at 750 ºC for 90, 300, and 510 s, respectively. The EDS analysis results of the heated Al–10 vol% $Al_{2.7}Ni_{0.3}Ti$ refiner are listed in Table VI. These figures reveal that heating for a short time causes the decomposition of the $Al_{2.7}Ni_{0.3}Ti$ phase into Al_3Ti and Al_3Ni phases. Namely, the complete decomposition of the $Al_{2.7}Ni_{0.3}Ti$ phase into Al_3Ti and Al_3Ni phases was found for the Al–10 vol% $Al_{2.7}Ni_{0.3}Ti$ refiner heated at 750 ºC for 90 s. On the other hand, in the case of the Al-10 vol% $Al_{2.7}Ni_{0.3}Ti$ refiner, no notable difference in microstructure between the unheated refiner and the refiner heated at 750 °C for 90 s was observed. [27] By comparing the decomposition phenomena in the Al-10 vol% $Al_{2.7}Ni_{0.3}Ti$ and Al-10 vol% $Al_{2.7}Fe_{0.3}Ti$ refiners, one can recognize that the thermal stability of the $Al_{2.7}Ni_{0.3}Ti$ phase in the refiner is lower than that of the $Al_{2.7}Fe_{0.3}Ti$ phase. This may be the reason for the relatively lower grain refinement performance of the Al-10 vol%$Al_{2.7}Ni_{0.3}Ti$ refiner. In this manner, the thermal stability of the heterogeneous nucleation site also affects the grain refinement performance.

4. Conclusions

In this study, the heterogeneous nucleation of α-Al primary crystal on the $L1_2$ modified $Al_{2.7}Ni_{0.3}Ti$ ($Al_{67}Ni_8Ti_{25}$) phase was investigated. A refiner with $L1_2$ modified $Al_{2.7}Ni_{0.3}Ti$ particles prepared by gas atomization was fabricated by SPS. The obtained results are summarized as follows.

1) Smaller grains are found for the Al cast manufactured with the Al-10 vol% $Al_{2.7}Ni_{0.3}Ti$ refiner. Therefore, $L1_2$ modified $Al_{2.7}Ni_{0.3}Ti$ particles can act as effective heterogeneous nucleation sites for primary Al in the solidification process. The maximum grain refinement performance can be achieved by the Al-10 vol% $Al_{2.7}Ni_{0.3}Ti$ refiner after the holding time of 690 s.

2) The grain refinement performance is relatively weaker than expected. This is because the Al-10 vol% $Al_{2.7}Ni_{0.3}Ti$ refiner does not have a high thermal stability. The thermal stability of the heterogeneous nucleation site also affects the grain refinement performance.

3) The mechanical properties of pure Al casts were improved by using the Al-10 vol% $Al_{2.7}Ni_{0.3}Ti$ refiner through grain refinement.

Acknowledgments

The authors are thankful for the financial support from The Light Metal Educational Foundation Inc. of Japan. This research was partially supported by the New Energy and Industrial Technology Development Organization (NEDO) of Japan, and by the Japan Science and Technology Agency (JST) under Industry-Academia Collaborative R&D Program "Heterogeneous Structure Control: Towards Innovative Development of Metallic Structural Materials".

References

1) A. Cibula, J. Inst. Met. **76**, 321 (1949-1950).
2) A. Cibula, J. Inst. Met. **80**, 1 (1951-1952).
3) F. A. Crossley and L. F. Mondolfo, Trans. AIME **191**, 1143 (1951).
4) I. Maxwell and A. Hellawell, Acta Metall. **23**, 901 (1975).
5) J. A. Marcantonio and L. F. Mondolfo, Metall. Trans. **2**, 465 (1971).
6) J. Kaneko, Keikinzoku **23**, 218 (1973) [in Japanese].
7) B. D. Warr, G. W. Delamore, and R. W. Smith, Metall. Trans. B **6**, 625 (1975).

8) P. S. Mohanty and J. E. Gruzleski, Acta Metal. Mater. **43**, 2001 (1995).
9) A. Ohno and H. Sôda, Nihon Kinzoku Gakkaishi **33**, 1049 (1969) [in Japanese].
10) M. Easton and D. StJohn, Metall. Mater. Trans. A **30**, 1625 (1999).
11) Z. Zhang, S. Hosoda, I. S. Kim, and Y. Watanabe, Mater. Sci. Eng. A **425**, 55 (2006).
12) H. Sato, K. Ota, H. Kato, M. Furukawa, M. Azuma, Y. Watanabe, Z. Zhang, and K. Tsuzaki, Mater. Trans. **54**, 1554 (2013).
13) K. Yamauchi, T. Kunimine, H. Sato, and Y. Watanabe, Mater. Trans. **56**, 99 (2015).
14) Y. Watanabe, T. Hirako, T. Chiba, and H. Sato, Keikinzoku **67**, 208 (2017) [in Japanese].
15) B. L. Bramfitt, Metall. Trans. A **1**, 1987 (1970).
16) K. Honda, K. Ushioda, W. Yamada, K. Tanaka, and H. Hatanaka, Mater. Trans. **49**, 1401 (2008).
17) M. Kato, M. Wada, A. Sato, and T. Mori, Acta Metal. **37**, 749 (1989).
18) M. Kato, Mater. Trans., JIM **33**, 89 (1992).
19) M. Kato, Testu-to-Hagane **78**, 209 (1992) [in Japanese].
20) Y. Watanabe, Q. Zhou, H. Sato, T. Fujii, and T. Inamura, Jpn. J. Appl. Phys. **56**, 01AG01 (2017).
21) Y. Watanabe, H. Eryu, and K. Matsuura, Acta Mater. **49**, 775 (2001).
22) H. Sato, Y. Noda, and Y. Watanabe, Mater. Trans. **54**, 1274 (2013).
23) K. Yamashita, C. Watanabe, S. Kumai, M. Kato, A. Sato, and Y. Watanabe, Mater. Trans. JIM **41**, 1322 (2000).
24) Y. Watanabe, P. D. Sequeira, H. Sato, T. Inamura, and H. Hosoda, Jpn. J. Appl. Phys. **55**, 01AG03 (2016).
25) P. Villars, *Pearson's Handbook Desk Edition Crystallographic Data for Intermetallic Phases* (ASM International, Materials Park, OH, 1997) Vol. 1, p. 382.
26) Y. Watanabe, T. Hamada, and H. Sato, Jpn. J. Appl. Phys. **55**, 01AG01 (2016).
27) Y. Watanabe, T. Hamada, and H. Sato, Jpn. J. Appl. Phys. **56**, 01AG02 (2017).
28) P. Villars and L. D. Calvert, *Pearson's Handbook of Crystallographic Data for Intermetallic Phases,* (ASM International, Materials Park, OH, 1985) Vol. 2, p. 1043.
29) Z. Zhang, X. Shen, C. Zhang, S. Wei, S. Lee, and F. Wang, Mater. Sci. Eng. A **565**, 326 (2013).

30) Y. J. Wu, R. Kimura, N. Uekawa, K. Kakegawa, and Y. Sasaki, Jpn. J. Appl. Phys. **41**, L219 (2002).

Figure Captions

Fig. 1. (Color online) XRD profiles of gas-atomized $Al_{2.7}Ni_{0.3}Ti$ particles (a) and Al-10 vol% $Al_{2.7}Ni_{0.3}Ti$ refiner (b).

Fig. 2. (Color online) SEM images showing $L1_2$ modified $Al_{2.7}Ni_{0.3}Ti$ particles prepared by gas atomization. Low-magnification photograph (a), powder surface (b), cross sections of particles (c), and high-magnification micrograph showing cross sections of particles (d).

Fig. 3. (Color online) SEM images showing Al-10 vol%$Al_{2.7}Ni_{0.3}Ti$ refiner. Low- (a) and high-magnification images (b).

Fig. 4. Grain refinement performance test results of the Al-10 vol% $Al_{2.7}Ni_{0.3}Ti$ refiner after holding times of 0 (a), 300 (b), 510 (c), 600 (d), 690 (e), and 780 s (f). Al cast without the refiner (g).

Fig. 5. (Color online) Average grain size of the samples with different holding times after addition of Al-10 vol% $Al_{2.7}Ni_{0.3}Ti$ refiner. The data of the Al-10 vol% $Al_{2.7}Fe_{0.3}Ti$ refiner obtained from Ref. 26 is also shown in this figure.

Fig. 6. (Color online) Nominal stress-nominal strain curves of Al casts manufactured without and with the Al-10vo% $Al_{2.7}Ni_{0.3}Ti$ refiner after a holding time of 690 s. The dimensions of the tensile specimen are also shown in this figure.

Fig. 7. (Color online) Microstructures of Al-10 vol% $Al_{2.7}Ni_{0.3}Ti$ refiner heated at 750 ^{o}C for 90 (a) and (a'), 300 (b) and (b'), and 510 s (c) and (c').

Table I. Plane disregistry and parameter *M* values of some crystallographic orientation relationships between Al_3Ti and Al.

	$[uvw]_{Al_3Ti}$	$[uvw]_{Al}$	$d[uvw]_{Al_3Ti}$	$d[uvw]_{Al}$	θ	$\cos\theta$	$d[uvw]_{Al_3Ti}\cos\theta$	δ	$\delta^{(hkl)_{Al_3Ti}}_{(hkl)_{Al}}$	Principal strain	M (x10^{-3})
$(100)_{Al_3Ti}//(100)_{Al}$	001	001	0.4304	0.4049	0	1	0.4304	6.30	3.95	0.0630	4.306
	$0\bar{2}1$	$0\bar{1}1$	0.5775	0.5726	3.18	0.998	0.5763	0.65			
	010	010	0.3851	0.4049	0	1	0.3851	4.89		-0.0489	
$(100)_{Al_3Ti}//(100)_{Al}$	001	001	0.8608	0.8098	0	1	0.8608	6.30	5.08	0.0630	4.306
	$0\bar{1}1$	$0\bar{1}2$	0.9430	0.9054	2.46	0.999	0.9421	4.05			
	010	010	0.3851	0.4049	0	1	0.3851	4.89		-0.0489	
$(001)_{Al_3Ti}//(001)_{Al}$	100	100	0.3851	0.4049	0	1	0.3851	4.89	4.89	-0.0489	6.377
	010	010	0.3851	0.4049	0	1	0.3851	4.89		-0.0489	
	$\bar{1}10$	$\bar{1}10$	0.5446	0.5726	0	1	0.5446	4.89			
$(110)_{Al_3Ti}//(110)_{Al}$	001	001	0.4304	0.4049	0	1	0.4304	6.30	4.11	0.0630	4.306
	$\bar{1}10$	$\bar{1}10$	0.5446	0.5726	0	1	0.5446	4.89		-0.0489	
	$\bar{2}21$	$\bar{1}11$	0.6941	0.7013	3.05	0.999	0.6934	1.13			
$(110)_{Al_3Ti}//(110)_{Al}$	001	001	0.8608	0.8098	0	1	0.8608	6.30	4.60	0.0630	4.306
	$\bar{1}10$	$\bar{1}10$	0.5446	0.5726	0	1	0.5446	4.89		-0.0489	
	$\bar{1}11$	$\bar{1}12$	1.0186	0.9918	2.94	0.999	1.0176	2.60			
$(112)_{Al_3Ti}//(111)_{Al}$	$\bar{1}10$	$\bar{1}10$	0.2723	0.2863	0	1	0.2723	4.89	2.78	-0.0489	2.240
	$\bar{1}\bar{1}1$	$\bar{1}\bar{1}2$	0.5093	0.4959	0	1	0.5093	2.70		0.0270	
	$0\bar{2}1$	$0\bar{1}1$	0.5775	0.5726	1.87	0.999	0.5769	0.75			
$(112)_{Al_3Ti}//(111)_{Al}$	$\bar{1}10$	$\bar{1}10$	0.5446	0.5726	0	1	0.5446	4.89	2.13		
	$0\bar{2}1$	$0\bar{1}1$	0.5775	0.5726	1.87	0.999	0.5769	0.75			
	$20\bar{1}$	$10\bar{1}$	0.5775	0.5726	1.87	0.999	0.5769	0.75			

Table II. EDS analysis results of the gas-atomized $Al_{2.7}Ni_{0.3}Ti$ particles shown in Figs. 2(b) and 2(d) (unit: mol%).

	Al	Ni	Ti
Theoretical value of $Al_{2.7}Ni_{0.3}Ti$	67.0	8.0	25.0
1 (Surface)	67.1	7.9	25.0
2 (Surface)	64.6	8.4	26.9
3 (Matrix)	63.1	6.7	30.2
4 (Secondary phase)	58.6	15.4	26.0

Table III. Volume fraction of secondary phase in the gas-atomized $Al_{2.7}Ni_{0.3}Ti$ particles with different sizes (unit: vol%).

Particle size of $Al_{2.7}Ni_{0.3}Ti$	32-75 μm	75-150 μm	150-212 μm
Volume fraction of secondary phase	6.9	8.0	8.8

Table IV. EDS analysis results of the Al-10 vol% $Al_{2.7}Ni_{0.3}Ti$ refiner shown in Fig. 3(b) (unit: mol%).

	Al	Ni	Ti
Theoretical value of $Al_{2.7}Ni_{0.3}Ti$	67.0	8.0	25.0
1 (Matrix)	99.9	0.0	0.1
2 (Matrix)	99.8	0.0	0.2
3 (Particle)	63.1	7.1	29.8
4 (Particle)	64.4	6.2	29.4

Table V. 0.2% proof stress and tensile strength evaluated from stress-strain curves, and Vickers hardnesses of Al casts manufactured with and without the Al-10 vol% $Al_{2.7}Ni_{0.3}Ti$ refiner.

	0.2% proof stress, $\sigma_{0.2}$ /MPa	Tensile strength, σ_{TS} /MPa	Vickers hardness, *HV*
Without refiner	20.1	40.1	14.3
With refiner (Holding time: 690 s)	26.4	56.9	15.8

Table VI. EDS analysis results of the heated Al-10 vol% $Al_{2.7}Ni_{0.3}Ti$ refiner shown in Fig. 7 (unit: mol%).

	Al	Ni	Ti	Phase
Theoretical value	67.0	8.0	25.0	$Al_{2.7}Ni_{0.3}Ti$
1	99.8	0.0	0.2	α-Al
2	75.7	0.0	24.3	Al_3Ti
3	73.6	26.3	0.2	Al_3Ni
4	99.1	0.0	0.9	α-Al
5	74.8	0.2	25.0	Al_3Ti
6	73.3	26.6	0.1	Al_3Ni
7	99.5	0.0	0.5	α-Al
8	73.3	0.5	26.2	Al_3Ti
9	81.9	17.9	0.2	

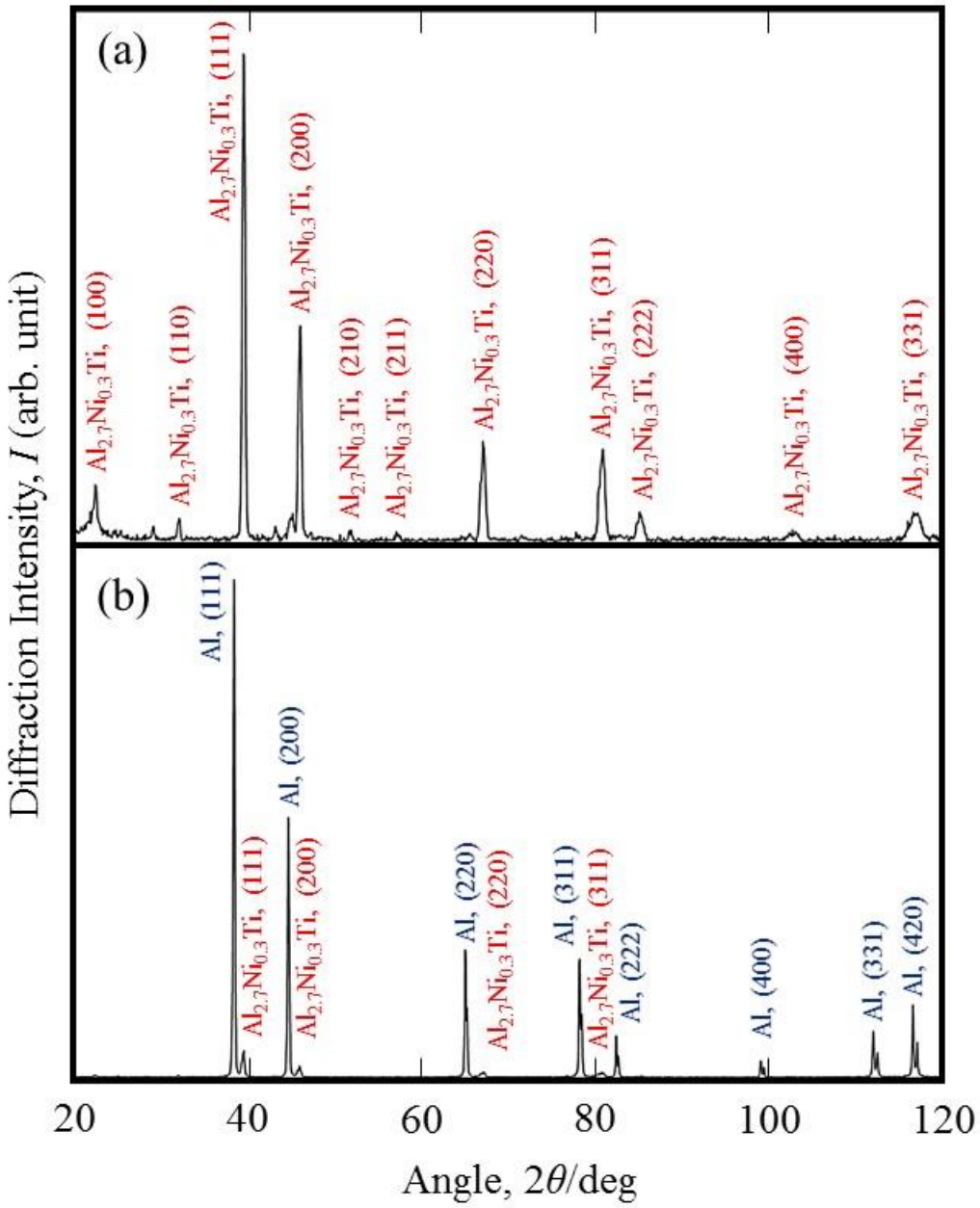

Fig. 1. (Color online) XRD profiles of gas-atomized $Al_{2.7}Ni_{0.3}Ti$ particles (a) and Al-10 vol% $Al_{2.7}Ni_{0.3}Ti$ refiner (b).

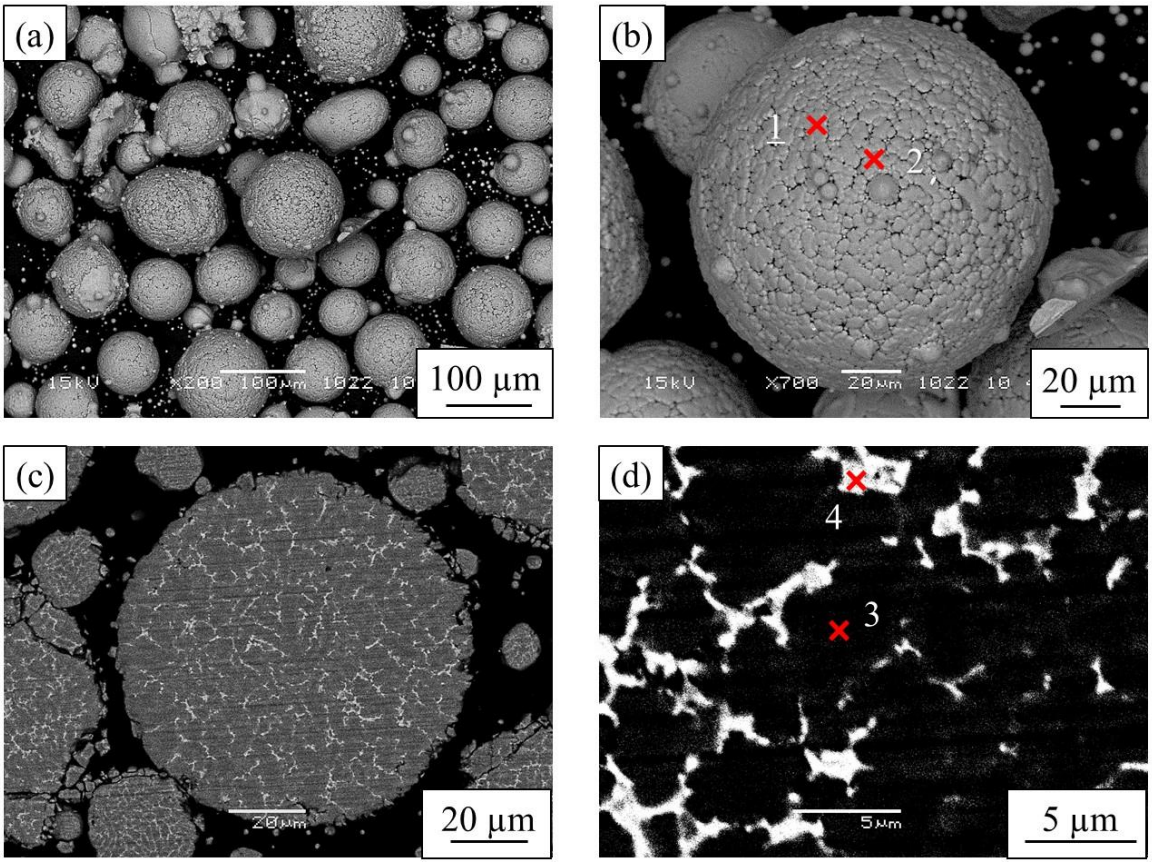

Fig. 2. (Color online) SEM images showing $L1_2$ modified $Al_{2.7}Ni_{0.3}Ti$ particles prepared by gas atomization. Low-magnification photograph (a), powder surface (b), cross sections of particles (c), and high-magnification micrograph showing cross sections of particles (d).

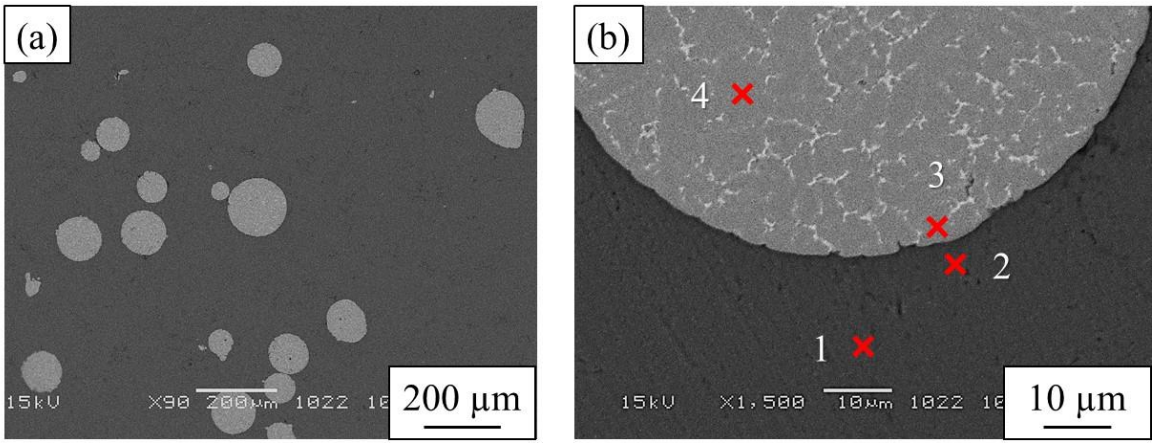

Fig. 3. (Color online) SEM images showing Al-10 vol%$Al_{2.7}Ni_{0.3}Ti$ refiner. Low- (a) and high-magnification images (b).

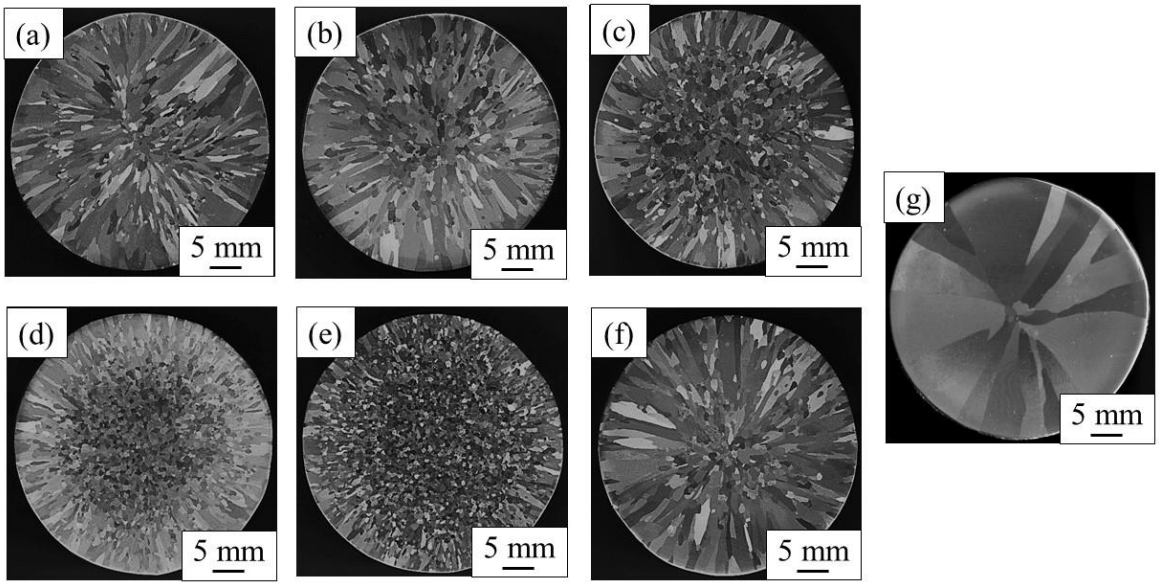

Fig. 4. Grain refinement performance test results of the Al-10 vol% $Al_{2.7}Ni_{0.3}Ti$ refiner after holding times of 0 (a), 300 (b), 510 (c), 600 (d), 690 (e), and 780 s (f). Al cast without the refiner (g).

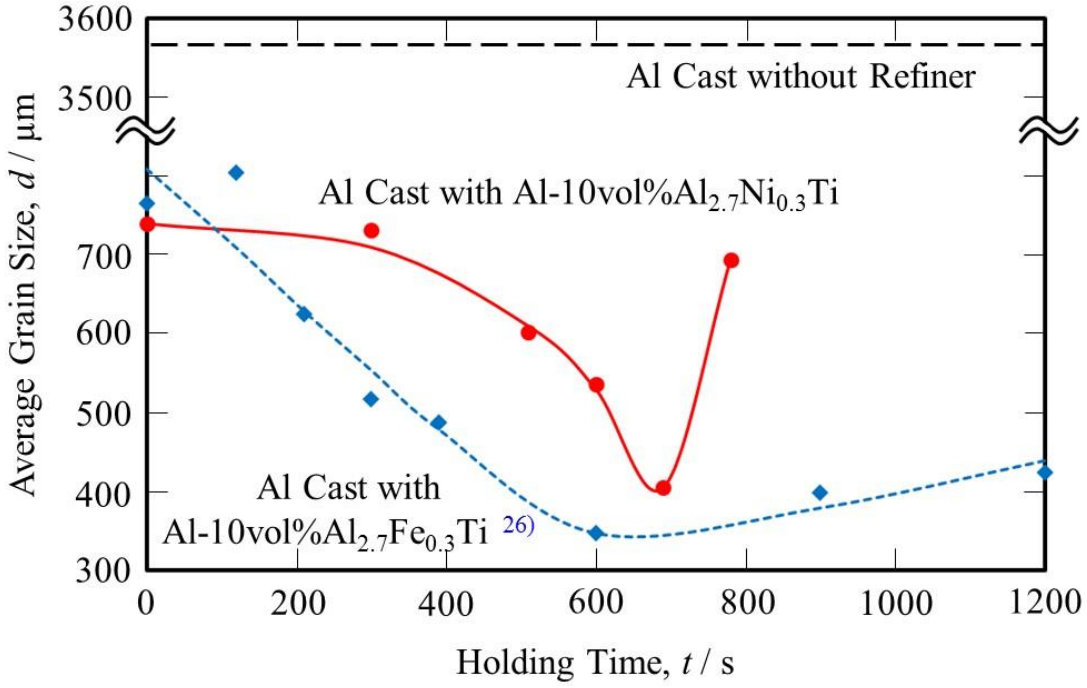

Fig. 5. (Color online) Average grain size of the samples with different holding times after addition of Al-10 vol% $Al_{2.7}Ni_{0.3}Ti$ refiner. The data of the Al-10 vol% $Al_{2.7}Fe_{0.3}Ti$ refiner obtained from Ref. 26 is also shown in this figure.

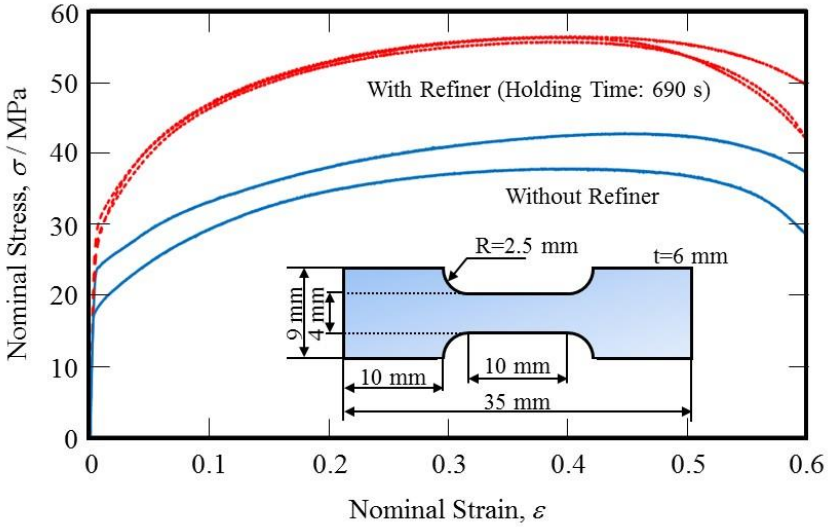

Fig. 6. (Color online) Nominal stress-nominal strain curves of Al casts manufactured without and with the Al-10vo% $Al_{2.7}Ni_{0.3}Ti$ refiner after a holding time of 690 s. The dimensions of the tensile specimen are also shown in this figure.

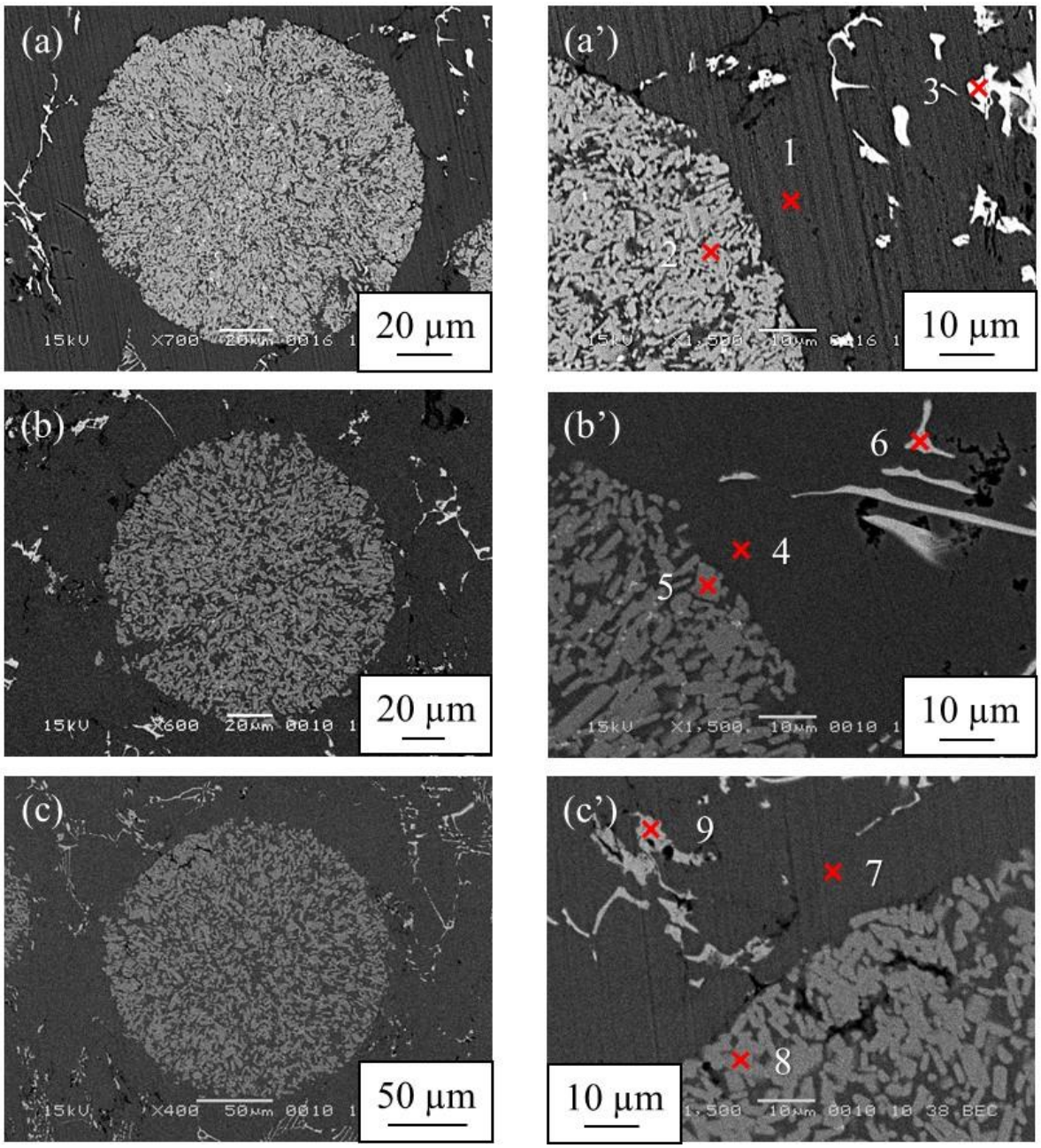

Fig. 7. (Color online) Microstructures of Al-10 vol% $Al_{2.7}Ni_{0.3}Ti$ refiner heated at 750 °C for 90 (a) and (a'), 300 (b) and (b'), and 510 s (c) and (c').